Materials and Design 197 (2021) 109187

Contents lists available at ScienceDirect

Materials and Design

journal homepage: www.elsevier.com/locate/matdes

Open-cell tungsten nanofoams: Scaling behavior and structural disorder dependence of Young's modulus and flow strength

Mingyue Zhao, Dr. [a,*], Karsten Schlueter [b,c], Michael Wurmshuber [a], Maria Reitgruber [a], Daniel Kiener [a]

[a] Chair of Materials Physics, Montanuniversität Leoben, Jahnstraße 12, 8700 Leoben, Austria
[b] Max-Planck-Institut für Plasmaphysik, Boltzmannstr. 2, D-85748 Garching, Germany
[c] Fakultät für Maschinenwesen, Technische Universität München, D-85748 Garching, Germany

HIGHLIGHTS

- Tungsten nanofoams with varied relative densities and cellular structures were investigated by depth-sensing nanoindentation
- High pressure torsion is an effective avenue in eliminating large cells and avoiding cells with strong shape anisotropy
- Nanoindentation properties of tungsten nanofoams with self-similar structures follow theoretical scaling equations
- Mechanical performance of tungsten foams can be tailored by adjusting cell thickness, cell shape and structural disorder

GRAPHICAL ABSTRACT

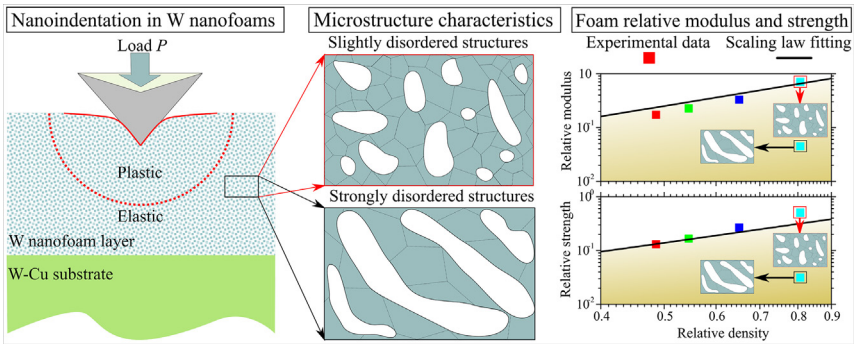

ARTICLE INFO

Article history:
Received 30 June 2020
Received in revised form 9 September 2020
Accepted 23 September 2020
Available online 26 September 2020

Keywords:
Nanoporous
Tungsten
Nanoindentation
Microstructure
Mechanical properties

ABSTRACT

Nanoporous metallic materials are of great interest to the scientific and industrial communities. To better tailor the mechanical properties to the functional needs, here we examined open-cell nanocrystalline tungsten nanofoams to provide fundamental insight into the correlations between cellular structures and mechanical properties. Depth-sensing nanoindentation tests were performed on tungsten nanofoams with independently varied relative densities and cellular structures to obtain foam mechanical properties. For tungsten nanofoams with self-similar and highly ordered cellular structures, the Young's modulus is insensitive to the ligament size, but varies with the relative density in a close way to the classical Gibson-Ashby scaling law. The flow strength of these regular nanofoams follows the classical scaling behavior only when properly taking into consideration the ligament size effect and corrections for the relative density. Contrarily, tungsten nanofoams with a certain relative density but varied cellular structures exhibit deterioration of both, Young's modulus and flow strength, with increasing structural disorders. This study emphasizes the importance of structural self-similarity when applying the established scaling laws to describe the foam mechanical properties. Meanwhile, it demonstrates that for optimized performance of the nanofoams, cellular architecture is the key factor of consideration.

1. Introduction

Metallic foams, i.e., porous metals, have been of great interest for a variety of applications in the past decades, since they provide a subtle

* Corresponding author.
E-mail address: mingyue.zhao@unileoben.ac.at (M. Zhao).

https://doi.org/10.1016/j.matdes.2020.109187

combination of the beneficial properties of both, metals and porous structures [1–6]. In contrast to the conventional macroscopic metallic foams, nanoporous (NP) metallic foams are significantly stronger because of size effects on material strength [7,8], and excellent in functional properties such as high radiation resistance due to the large density of defect sinks represented by the free surfaces [9–11]. As a material with the highest melting point among metals, a high atomic mass, a low coefficient of thermal expansion and superior strength, tungsten (W) is presently considered as top candidate for plasma-facing shield component and as structural component in nuclear reactor facilities (e.g. fusion DEMO designs) to withstand the extreme environments (e.g. high temperatures, extreme irradiation) for protecting personnel and sensitive equipments [12]. However, novel materials are in great demand in the next generation nuclear reactors, as the existing W materials are hardly to resist the microstructural damage and the consequent mechanical properties degradation when exposed to extreme neutron or ion particle irradiation [13–15]. Nanoporous W foams are ideally suited as such a novel material to achieve the potential of extraordinary strength and concurrent radiation tolerance, as they possess both the beneficial properties of W and the positive attributes of nanoporous foams.

The great interest in the technological potential of NP metals strongly promoted fundamental research related to the structure-property correlations of this material class. In material science, a general rule of mixtures provides theoretical upper- and lower- bounds on various mechanical properties by applying the Voigt (i.e., axial loading) and Reuss (i.e., transverse loading) models for a composite, respectively [16,17]. A porous material can be treated as a special case of a two-phase composite, in which the mechanical properties of one phase is equal to zero. Therefore, the rule of mixtures for elastic modulus and yield strength of porous W takes the forms given in Table 1. It is seen that the Voigt upper bound shows a linear dependence of foam mechanical properties on relative density. In 1980s, Gibson and Ashby (GA) unveiled power-law relationships (see Table 1) between relative density (ratio between the density of a foam and of a solid metal, φ) and mechanical properties for open-cell macroscopic foams (ligament thickness $t>>$ 500 nm) by using a cubic unit cell model, which describes the porous structure as a regular and periodic three-dimensional (3D) arrangement of connected beams with a square cross-section and very small thickness to free/unsupported length (t/l) ratios [18,19]. Theoretical analysis based on this model suggested that there are three regimes of foam deformation behavior: at low relative densities ($\varphi < 0.3$) the material can be modeled as a network of bending beams, while at high relative densities ($\varphi > 0.8$) it behaves like a solid with widely separated spherical holes. At intermediate densities ($0.3 \le \varphi \le 0.8$), the material performs neither as a network of bending beams, nor as a solid with isolated holes in it. Although distinct deformation mechanisms occur, a square law relationship $E_f = E_s\varphi^2$ applies to open cell foams over a wide range of relative densities from 0.01 to 1.00. Here, E is Young's modulus, while subscripts s and f represent for solid and foam metals, respectively. The calculation of the plastic yielding stress of open-cell foams (σ_f) is based on the formation of plastic hinges at the ends of the cubic cell members [18,19], which results in σ_f being proportional to $\varphi^{3/2}$, giving $\sigma_f = 0.3\sigma_s\varphi^{3/2}$. However, this equation is valid only at low relative densities ($\varphi < 0.6$). When the relative density becomes larger, the cubic model is no longer a good approximation for the cell shape, as the open cell foams tend to have more volume at the cell corners [20]. Moreover, axial deformation occurring over the entire length ($t + l$) of the solid cell members becomes increasingly important at high relative densities. Under this concern, GA employed a refined cell model (pentagonal dodecahedral cell shape) to recalculate the foam properties (see Table 1). Years later, this conceptual framework provided by the GA cubic model was used to connect the mechanical properties of NP metals with their morphological features [21–23]. Here, NP metals exhibit a structure in which mass agglomerates at ligament junctions and ligaments have large t/l ratios [24]. A size-dependent behavior of Young's modulus for open-cell nanoporous metals has been revealed through analytical modelling [25], molecular dynamics simulation [26] and experiments [24,25,27]. That is, the open-cell NP metals show a drastic rise in Young's modulus when decreasing the ligament size below 10 nm, but behave as conventional macroscopic foams for ligament sizes above 20 nm. This stiffening of NP metals with sub-10 nm ligaments is ascribed to the impact of surface stress states [28]. In terms of yield strength, a strong discrepancy between experimental data and GA model predictions was found, giving rise to various attempts to rationalize the observed differences by certain modifications to the GA scaling equations without changing the fundamental assumptions, i.e., the aggregation of mass at ligament junctions is negligible and the ligaments are with very small t/l ratios [21,22,29]. From the research on nanoporous Au foams, Hodge (H) et al. revealed that the yield strength of the individual ligaments (σ_{lig}) is dependent on the ligament thickness t, which was related to the Hall-Petch-like equation ($\sigma_{lig} = \sigma + kt^{-1/2}$) [21]. Accounting Hall-Petch-like behavior of individual ligaments, the GA scaling law for yield strength is modified to $\sigma_f = 0.3\varphi^{3/2}(\sigma + kt^{-1/2})$ (hereinafter referred to as GA-H scaling law), which can be accurately applied to NP metals with a relative density lower than 0.3 [21]. At even higher relative density ($\varphi > 0.3$), the contribution of ligament junctions to relative density becomes significant. Fan and Fang (FF) refined the GA scaling law after Hodge et al. into $\sigma_f = 0.23\varphi^{3/2}(1 + \varphi^{1/2})(\sigma + kt^{-1/2})$ (referred to as GA-FF scaling law) for NP metals of higher φ by incorporating corrections to the density equation [30].

In our previous work, we established a unique fabrication route to create open-cell nanocrystalline nanoporous tungsten with a relative density of 0.65 and an average ligament size of 25 nm [31]. Depth-sensing nanoindentation measurements showed that the elastic modulus of this particular W nanofoam agrees well with the classical GA scaling law and its flow strength can be reasonably explained by the modified scaling law proposed by Fan and Fang [30]. Notably, the good correlation between experimental data and scaling law predictions was based on a full data set for a certain structure and density, the full potential and possible limitations of the established scaling laws in describing W foam properties is therefore not yet explored. Structural disorders, arising from non-periodicity of solid cell arrays [32], uneven distribution of solids [33], coalescence of solid cells [34], solid cell irregularity [35], etc., were reported to have great influence on the mechanical properties of open-cell foams. Thus, for a rigorous study, in the present work the mechanical properties of different W nanofoams with independently varied relative densities and cellular

Table 1
Summary of mechanical behavior of three-dimentional open cell cellular materials.

	Relative density φ	Modulus E_f	Yield strength σ_f	Ref.
Rule of Mixtures		$0 < E_f \le \varphi E_s$	$0 < \sigma_f \le \varphi\sigma_s$	[16,17]
GA simple scaling law	$\varphi = (t/l)^2$	$E_f = E_s\varphi^2$	$\sigma_f = 0.3\sigma_s\varphi^{3/2}$	[18]
GA refined scaling law	$\varphi = \frac{(t/l)^2 + 0.766(t/l)^3}{0.766(1+t/l)^3}$		$\sigma_f = C\sigma_s\frac{(t/l)^3}{(1+t/l)^2}$ (for low φ) $\sigma_f \approx \sigma_s\frac{(t/l)^2}{(1+t/l)^2}$ (for high φ)	[20]
GA-H scaling law	$\varphi = (t/l)^2$		$\sigma_f = 0.3\varphi^{3/2}(\sigma + kt^{-1/2})$	[21]
GA-FF scaling law			$\sigma_f = 0.23\varphi^{3/2}(1 + \varphi^{1/2})(\sigma + kt^{-1/2})$	[30]

structures (especially the structural disorders of the foam) were investigated and compared to the established scaling law predictions. We unveiled that to rationalize the occurring discrepancies, the impact of cellular structures on the mechanical properties of the open-cell W have to be accounted for.

2. Experimental

2.1. Precursor synthesis

The nanoporous W samples examined in the present study were made by reverse phase dissolution of nanocrystalline (NC) $W_{100-x}Cu_x$ precursors (where x = 10, 20, 28 and 33 wt%, corresponding to a Cu content of 19.3, 35.0, 45.5, 51.4 vol%). The approach to fabrication of the NC $W_{100-x}Cu_x$ precursors is via high pressure torsion (HPT) of coarse-grained (CG) $W_{100-x}Cu_x$ composites purchased from Goodfellow (*England*) and provided by Plansee (*Austria*). HPT was conducted at room temperature and an applied pressure of 7.5 GPa with a rotational speed of 1.2 rpm on CG composite discs with a diameter of 8 mm and a thickness of 0.8–0.9 mm. A detailed introduction to the HPT processing of immiscible W–Cu composite systems can be found in Refs. [36,37]. The equivalent strains applied to different radii of the CG composite discs can be evaluated by $\varepsilon = 2\pi rn/\sqrt{3}t$ [38]. Here n is the rotation number, r is the sample radius, and t is the sample thickness. Prior to foam creation, the produced NC W–Cu precursors were heat treated in a vacuum furnace at 300 °C for 1 h to reduce the amount of mechanical mixing between W and Cu induced during the HPT procedure [36].

2.2. Foam creation

Reverse phase dissolution of the NC W_xCu_{100-x} precursors to create NP W foams was conducted in an ammonium persulfate ($(NH_4)_2S_2O_8$) aqueous solution at room temperature. Reverse phase dissolution, i.e., selectively removing the more noble element Cu, was proceeded by just immersing the heat treated HPT disk (with one side mirror polished) into the etching solution for 8 days. For a detailed description on the foam creation procedure, the dissolution mechanism and microstructural evolution of NC precursors during dissolution, please refer to Ref. [31]. The reverse phase dissolution procedure results in a dissolution of Cu from the polished surface to a depth of ~15 μm for the NC $W_{80}Cu_{20}$ precursor [31], which is over 6 times deeper than the subsequent nanoindentation experiments will probe. Since all Cu phase was locally removed and there was no detectable grain growth or reconstruction during the dissolution process [31], the density of the created foams (ρ_f) was calculated using the following equation:

$$\rho_f = \frac{w_W}{\frac{w}{\rho_W} + \frac{w_{Cu}}{\rho_{Cu}}} \quad (w_W + w_{Cu} = 1) \tag{1}$$

where w and ρ represent the mass fraction and density of one phase in a composite. The relative density of porous W (φ) listed in Table 2 was then calculated by $\varphi = \rho_f/\rho_W$. The porosity of porous W (ϕ) is equivalent to $(1-\varphi)$. Please note that the equations given here are only suitable for an ideal situation, in which the created W foams are completely Cu-free. In the real cases, the created W foams may contain a certain amount of Cu, resulting in an increase of the foam relative density and thereby impacting the mechanical properties of these foams. In the Supplemental Methods, the equations taking into account the removal fraction of Cu (q) are provided. The remaining of Cu will lead into an increase in the foam relative density for about $\frac{(1-q)\cdot w_{Cu}}{w_W} \times 100\%$.

Table 2
Basic information of the foams created from the nanocrystalline W—Cu precursors.

Foam	Precursor (in wt%)	Foam relative density (φ)	Foam porosity (ϕ)
$W_{0.807}$	$W_{90}Cu_{10}$	0.807	0.193
$W_{0.651}$	$W_{80}Cu_{20}$	0.651	0.349
$W_{0.545}$	$W_{78}Cu_{28}$	0.545	0.455
$W_{0.486}$	$W_{67}Cu_{33}$	0.486	0.514

2.3. Microstructure characterization

The microstructure is characterized on a large scale by a scanning electron microscope (SEM, *LEO 1525, Carl Zeiss GmbH, Germany*), and in detail employing a transmission electron microscope (TEM, *CM12, Philips, Netherlands*) operating at 120 kV. Prior to SEM observation, the surfaces of the NC W_xCu_{100-x} precursors were subjected to mechanical grinding by SiC paper and chemo-mechanical polishing by silicic acid solution. Thus, the polished surface of the porous metals was obtained by polishing the NC precursors before etching. TEM samples were prepared by mechanical polishing, dimpling with diamond paste and final Ar ion milling. The phase constitution in the TEM analyzed regions was identified from selected area electron diffraction (SAED) patterns. To determine the overall elemental compositions of the created foams, an energy dispersive X-ray spectrometer (EDX) consisting of an Oxford Ultim® Extreme detector was used.

2.4. Nanoindentation tests

The mechanical characteristics, including hardness (H), reduced Young's modulus (E_r), and deformation behavior under compressive stress, were obtained by depth-sensing nanoindentation using a G200 Nanoindenter (*KLA Corporation, USA*) equipped with a Berkovich tip (*Synton-MDP, Switzerland*, radius: ~170 nm according to Oliver-Pharr calibration [39]). The surfaces for nanoindentation tests were polished before reverse phase dissolution. A minimum of four nanoindentation tests with a spacing of about 50 μm between them were conducted on each specimen to ensure test accuracy and to minimize experimental errors. All nanoindentation tests were performed at a constant strain rate of 0.05 s^{-1}. A plastic zone develops during each indentation test, the size of which is generally believed to be approximately 5 times the depth of the indent for most conventional metals [40,41] and even smaller in porous metals because the deformation can be accommodated in a smaller volume due to densification [42]. To ensure that the nanoidentation on the foam layer does not oversample the bulk W–Cu substrate, the maximum penetration depth (h_m) of the Berkovich indenter was set to 2.5 μm for each indentation test. To mitigate the impact of thermal drift on the calculation of mechanical properties from the load-displacement curves, thermal equilibrium was established before each indentation test. At the maximum peak load (P_m), a 5 s holding was applied to minimize any creep or viscoplastic effects before the indenter was unloaded. During nanoindentation tests, E_r and H were tracked as a function of the indentation depths by using the continuous stiffness measurement (CSM) method. The residual indentation impressions were observed afterwards using the SEM.

Young's moduli of W foams (E_f) were determined from E_r based on the standard expression of the nanoindentation theory [39]:

$$\frac{1}{E_r(\varphi)} = \frac{1-\upsilon_d^2}{E_d} + \frac{1-\upsilon_f^2(\varphi)}{E_f(\varphi)} \tag{2}$$

Here, E_d and υ_d represent for the elastic modulus and Poisson's ratio of diamond, respectively, i.e., $E_d = 1140$ GPa and $\upsilon_d = 0.07$. The value of υ_f and E_f can be analytically estimated by using the equations derived from the differential effective medium approach (DEMA) for a concentrated two-phase pore-solid composite [43]. As shown in Table 3, four models were developed by Pal according to this DEMA approach [43]. Out of the four models, models 1 and 2 predict the υ_f and E_f to be a function of only porosity ϕ. They are expected to describe the υ_f and E_f at low to moderate values of porosity ϕ. The remaining two models, which

Table 3
Models and related equations for predicting the elastic modulus E_f and Poisson's ratio υ_f of W foams. E_s and υ_s are the elastic modulus and Poisson's ratio of the parent material without porosity, i.e., $E_s = 405$ GPa and $\upsilon_s = 0.28$ for solid W.

Model no.	$\upsilon_f(\phi)$	$E_f(\phi)$
1	$(1+\upsilon_s)\exp(-\phi/4)-1$	$E_s \exp(-23\phi/12)$
2	$(1+\upsilon_s)(1-\phi)^{1/4}-1$	$E_s(1-\phi)^{23/12}$
3	$(1+\upsilon_s)\exp(-\frac{\phi/4}{1-\phi/\phi m})-1$	$E_s \exp(-\frac{23\phi/12}{1-\phi/\phi_m})$
4	$(1+\upsilon_s)(1-\phi/\phi_m)^{\phi_m/4}-1$	$E_s(1-\phi/\phi_m)^{(23/12)\phi}{}_m$

incorporate the so-called 'crowding effect' of pores at high values of porosity ϕ, contain an additional parameter, the maximum packing volume fraction of pores ϕ_m. As ϕ_m is sensitive to pore structures (e.g. size, shape and orientation of pores), these two evolved models are capable of taking into account the effect of pore structures on the υ_f and E_f of pore-solid composites. In the case of W nanofoams covering a broad range of porosities, the model providing the best description of E_f calculated using Eq. (2) will be further employed to estimate the values of υ_f. For more related details, please see Sect. 3.2.

The strength of foams (σ_f) was assessed from the hardness values by employing an empirical equation:

$$\sigma_f = \frac{H}{C^*} \tag{3}$$

Here, C^* is a constraint factor. Its value strongly depends on the Poisson's ratio of the investigated W foams υ_f [18], i.e., C^* increases rapidly from unity toward the standard value of 3 when υ_f increases from zero to 0.28. Based on such a relationship, C^* is roughly estimated for each W nanofoam case (see Sect. 3.2). The strength in Eq. (3) was suggested to represent yield strength for ideally plastic materials, flow strength for work-hardening metals, or ultimate tensile strength for materials such as metallic glasses and ceramics. As introduced in Sect. 3.2, all W nanofoams follow an elastic-plastic deformation behavior. The hardness is measured when a fully developed plastic zone is achieved, i.e., from the plateau region of a hardness-displacement curve. Thus, the strength determined from Berkovich hardness by Eq. (3) will be discussed in the following as flow strength for the investigated W nanofoams.

3. Results

3.1. Microstructure of precursors and foams

Fig. 1 shows the microstructure of NC $W_{100-x}Cu_x$ precursors with varying densities and NC $W_{90}Cu_{10}$ precursors with varying structures. Note that all of the microstructural images were taken from the polished surfaces of HPT deformed samples. The saturated NC structures of the $W_{67}Cu_{33}$, $W_{72}Cu_{28}$ and $W_{80}Cu_{20}$ precursors were achieved at radii ranging from ~0.5 to 4 mm after a deformation of 60–80 turns. A substantial decrease of the W and Cu grain sizes and a significant improvement in the mutual distribution of the W and Cu phases are clearly noticed due to the HPT deformation. High resolution TEM analysis in our previous work [31] revealed that the W solids in the NC W–Cu precursors are well connected by either sharp and low-defective W/W grain boundaries (GBs) or very narrow (~1–3 nm) and Cu-decorated W/W GBs. As compared to the undeformed CG $W_{100-x}Cu_x$ composites, in which the W particles are almost completely separated by ductile Cu phase, the W phase in the deformed NC $W_{100-x}Cu_x$ (Figs. 1a–c) has an extraordinary good contiguity. Such beneficial impacts of deformation can also be observed in the $W_{90}Cu_{10}$ specimen, which exhibits a microstructure gradually refined and homogenized with increasing deformation strains (Figs. 1d–1h). As reported in Refs. [36, 37], before reaching a saturation regime, immiscible W–Cu composites beneath the sample surface (i.e. along the sample cross-section) exhibit a heavily elongated morphology in the shearing direction (i.e. in the direction parallel to the sample surface). Though a fully saturated state was not reached after a deformation of 140 turns, the $W_{90}Cu_{10}$ precursor with a deformation strain of about 3700 ($\varepsilon \approx 3700$) exhibits a microstructure almost as fine and as homogeneous as all the other $W_{100-x}Cu_x$ precursors (Figs. 1a–c). Thus, the NC $W_{100-x}Cu_x$ precursors shown in Figs. 1a–d are regarded as nanocomposites with self-similar and highly ordered structures.

Fig. 2a and b show bright field (BF) TEM images of the $W_{0.651}$ and $W_{0.807}$ nanofoams created from NC $W_{80}Cu_{20}$ in the saturated region and from NC $W_{90}Cu_{10}$ with $\varepsilon \approx 3700$, respectively. No Cu phase is detected in the SAED patterns (Fig. 2c), indicating the complete removal of Cu in the observed TEM regions. The W grains (dark contrasts) in the two nanofoams are comparable in size, about 20 nm on average. In the $W_{0.651}$ nanofoam, pores (bright contrasts) with elliptical and spherical morphologies co-exist, resulting in a dispersed pore size distribution ranging from ~5 to ~50 nm. The pores in the $W_{0.807}$ nanofoam

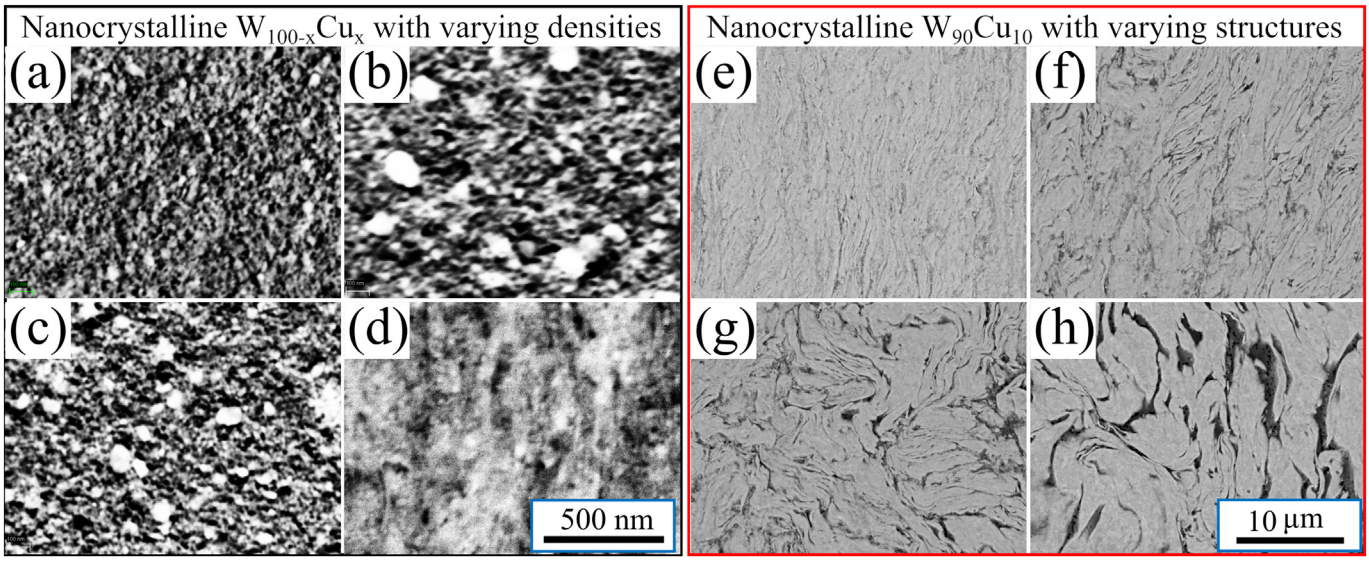

Fig. 1. Back-scattered electron (BSE) images of nanocrystalline $W_{100-x}Cu_x$ precursors with varying densities (a–d) and nanocrystalline $W_{90}Cu_{10}$ precursors with varying structures (e–h): (a) $W_{67}Cu_{33}$, (b) $W_{72}Cu_{28}$, (c) $W_{80}Cu_{20}$, (d) $W_{90}Cu_{10}$ with $\varepsilon \approx 3700$, (e) $\varepsilon \approx 2770$, (f) $\varepsilon \approx 1850$, (g) $\varepsilon \approx 930$, (h) $\varepsilon \approx 140$. The bright contrasts represent W while the dark contrasts are Cu.

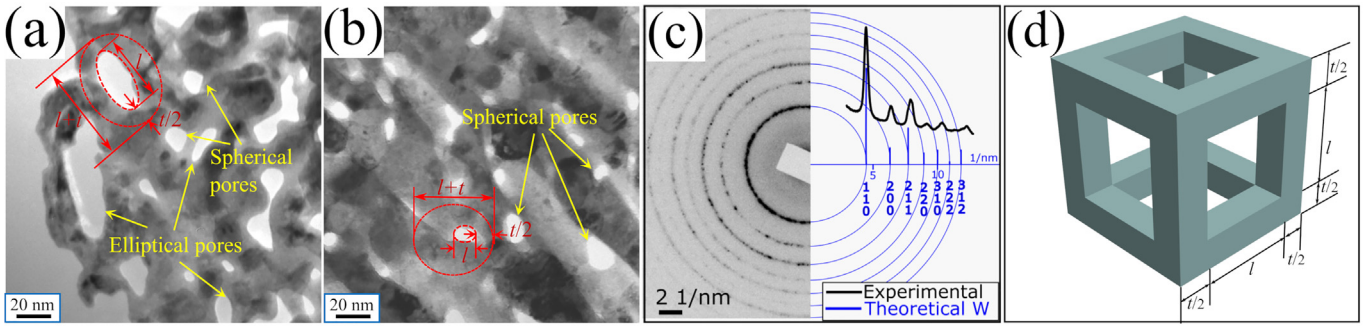

Fig. 2. Bright field TEM images of the (a) $W_{0.651}$ and (b) $W_{0.807}$ nanofoams created from NC $W_{80}Cu_{20}$ in the microstructure saturated region and from NC $W_{90}Cu_{10}$ with $\varepsilon \approx 3700$, respectively. Pores in (a) and (b) are shown as bright contrasts while the W grains exhibit dark contrasts. The materials in (a) and (b) have similar SAED patterns given exemplarily in (c). The method to determine the free/unsupported ligament length l and thickness t is illustrated in (d).

are mainly spherical and have a relatively narrow size distribution. Influenced by the pore shape, the shape anisotropy of W solid cells (indicated by the red dashed annular lines) in the $W_{0.651}$ nanofoam is greater than in the $W_{0.807}$ nanofoam. The $W_{0.651}$ nanofoam has on average a ligament thickness (t) of ~25 nm and a free/unsupported ligament length (l) of ~20 nm, resulting in a t/l ratio of 1.25. The average t and l in the $W_{0.807}$ nanofoam are about 28 and 12 nm, respectively, corresponding to a t/l ratio of 2.33. Note that t and l are determined based on GA's cubic cell model (see Fig. 2d). The BF-TEM images for the $W_{0.486}$ and $W_{0.545}$ nanofoams are not given here, as the preparation of TEM specimens turned out to be very challenging. Many cracks formed during Ar ion milling and consequently resulted in fragmentation of the TEM specimen. The inducement of the cracks is probably correlated with their t/l ratios, which are supposed to be smaller than 1.25. SEM images of surfaces or cross-sections with high magnifications (see Fig. S1 for an insight image) may serve as ideal substitutions of TEM images to unveil the porous features of the $W_{0.486}$ and $W_{0.545}$ nanofoams. However, they are also not provided for the following two reasons: (i) the surfaces exhibit a high level of roughness after the removal of Cu (see Fig. S1a), making the porous structures very obscure; (ii) a strong curtaining caused by high porosities happened to the $W_{0.486}$ and $W_{0.545}$ nanofoams during the focused ion beam (FIB) milling (see Fig. S4), making it challenging to take SEM images truly revealing their nanosized porous features.

3.2. Microstructure of residual indent impressions and compositional analysis

Fig. 3 displays the cellular structures of the $W_{0.807}$ foams created from NC $W_{90}Cu_{10}$ precursors with different deformation strains (a–e) and of the $W_{0.486}$ nanofoams created from NC $W_{67}Cu_{33}$ precursor in the saturated region (f). The $W_{0.545}$ and $W_{0.651}$ nanofoams have comparable cellular structures to the $W_{0.486}$ nanofoam. Fig. 3a' indicates measurement of the W ligament thickness t. It is observed that, with increasing deformation strains, structural disorders of the $W_{0.807}$ foams decreases, and meanwhile the thickness of the W ligaments decreases substantially from ~3.64 ± 2.37 μm to ~28 ± 7 nm. Since neither detectable grain growth nor grain reconstruction is involved in the foam-forming process [31], the elongated ligament morphology in the $W_{0.807}$ foams created from NC $W_{90}Cu_{10}$ precursors with deformation strains between 140 and 2770 (hereinafter $W_{0.807}$ foams with $140 \le \varepsilon \le 2770$ is used for simplicity) is well preserved. As speculated from Refs. [36, 37] and revealed from the SEM images of the cross-sections (see Figs. S7 and 8), these W ligaments are elongated in the direction parallel to the sample surfaces. The pores formed as a result of

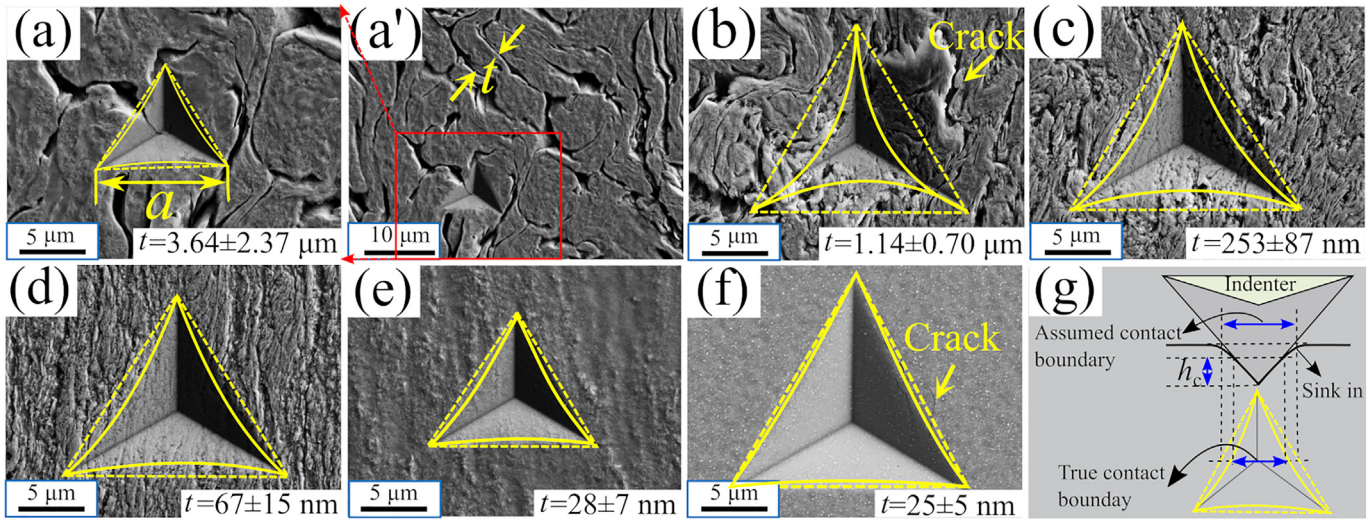

Fig. 3. Cellular structures and residual indentation impressions corresponding to the $W_{0.807}$ foams with increasing deformation strains (a) $\varepsilon \approx 140$, (b) $\varepsilon \approx 930$, (c) $\varepsilon \approx 1850$, (d) $\varepsilon \approx 2770$ and (e) $\varepsilon \approx 3700$, and to the $W_{0.486}$ nanofoam in the saturated region (f). (a') is a low magnification image of (a), showing how the ligament thickness t was determined. (g) is a schematic plot of a residual indentation impression with a sink-in morphology around a Berkovich indenter. The symbol a in (a) represent for the contact length of the indenter. SEM images clearly differentiating the cracks and indenter-material boundaries in (b) and (f) are available in Fig. S2. Quantitative elemental composition analysis of the surfaces and cross-sections by EDX can be found in Figs. S3–5.

selective removal of the Cu phase also exhibit pronounced shape anisotropy (see also Figs. S7 and 8). It is evident that, owing to the structural refinement induced by deformation, the surface topology becomes smoother with increasing deformation strains. Residual indent impressions after nanoidentation tests on these foams are also seen in Fig. 3. As depicted in the schematic plot (Fig. 3g), all foams exhibit residual indent impressions with a sink-in contact profile. Only in some cases (Fig. 3b and f), cracks formed due to the breaking of W ligaments are observed in the vicinity of indenter-surface contact boundaries. It is worth to mention here that, influenced by a self-similar structure, the residual indent impressions on the $W_{0.545}$ and $W_{0.651}$ nanofoams are similar to the one on the $W_{0.486}$ nanofoam (Fig. 3f).

The analysis of SAED patterns acquired from the TEM analyzed regions unveils a complete removal of Cu in the created $W_{0.651}$ and $W_{0.807}$ nanofoams. However, as a technique to identify the elemental compositions, SAED has its own limitations. First, the analyzed areas are only about several hundred nanometers in size. Second, the analysis of a TEM specimen may not reveal the real phase constitutions in the created W foams, as Cu is easier to mill than W during the preparation of TEM specimens by Ar ion milling. Therefore, the elemental compositions of the created W foams were also determined by EDX. The relevant EDX data are provided in Figs. S3–6. It is found that about 4.9 wt% Cu exists in the $W_{0.807}$ foam with $\varepsilon \approx 3700$, meaning that ~50% Cu was removed from the $W_{90}Cu_{10}$ precursor; for all the other W foams, a removal of over 90% Cu from the corresponding $W_{100-x}Cu_x$ precursors was detected. A detailed EDX analysis of the sub-surface (see Figs. S3c and 6) suggests that the disconnected Cu networks are responsible for the low removal rate of Cu in the $W_{0.807}$ foam with $\varepsilon \approx 3700$. The incomplete removal of Cu results in a 5.4% increase of the relative density of the $W_{0.807}$ foam with $\varepsilon \approx 3700$. For all the other W foams, the increase of relative density is within the range from 0.5 to 4.4%, which is comparatively insignificant.

3.3. Nanoindentation of the foams

Fig. 4a shows representative load-displacement indentation curves of the $W_{0.807}$ foams with various deformation strains and the $W_{0.486}$ nanofoams in the saturated region. During unloading, a reduction in penetration depth is observed, unveiling the elasto-plastic nature of the investigated W foams. The sink-in indent characteristics observed in Fig. 3 are ruled by the elasto-plastic deformation mechanisms of the W foams. The ratio between the penetration depths at complete unloading h_f and at maximum peak load h_m, which can easily be extracted from the unloading curve, is reported to be a useful indicator of the indent characteristics [44]. A large h_f/h_m ratio usually represents a low level of elastic relaxation in the unloading process. As seen in Fig. 4b, the h_f/h_m ratios of the W nanofoams with a self-similar and highly ordered structure decrease with increasing relative densities. In general, these nanofoams are very plastically deformable, as their h_f/h_m ratios are all above 0.7. For the $W_{0.807}$ foams, a substantial increase from 0.55 to above 0.7 is observed when the foam structures are getting more refined and periodic. As depicted in Fig. 4c, though with identical penetration depths at the maximum peak load P_m, due to different levels of elastic relaxation, the residual indent impression on the $W_{0.807}$ foam with $\varepsilon \approx 140$ has a contact length of the indenter a much smaller than on the $W_{0.807}$ foams with $\varepsilon \approx 930$ and 1850 (see Fig. 3). The levels of elastic relaxation for the $W_{0.807}$ foams with $\varepsilon \approx 930$ and 3700 are quite comparable (see Fig. 4b), the observed difference in the size of residual indent impressions (see Fig. 3) is originated from their different h_m values (see Fig. 4a). Please note that the variation of h_m values resulted from the load limit of the instrument (~670 mN) being reached before the set h_m of 2.5 μm for the $W_{0.807}$ foams with $\varepsilon \approx 2770$ and 3700.

The reduced Young's modulus E_r and hardness H values versus displacements are displayed in Fig. 5. The overlapped individual indentation curves for each W nanofoam case demonstrate a good reproducibility of the nanoindentation tests. Considering that the foam structures are not present in some cases to depths exceeding ~15 μm (see Ref. [31] and Figs. S3–4), only the indentation curves to displacements below 1 μm, where the mechanical influence from the NC W–Cu substrates is almost negligible, are displayed in Fig. 5. At indentation depths smaller than 250 nm, a noticeable scattering in the values of both E_r and H is observed, which could be induced by the indentation size effect [45,46], but most likely emerges from contact imperfections. Probably due to the local densification of the nano-ligaments under the indenter, a slight increase in E_r is noticed for indentation depths above 500 nm (Fig. 5a). As expected, this is least pronounced for the most dense foams. To account for this characteristic, the E_r and H values reported herein were measured at depths 250–500 nm and 500–1000 nm, respectively, where there is negligible depth dependence. Afterwards, E_f and σ_f of the foam were determined from the measured E_r and H values by using Eqs. (2) and (3), respectively.

The assessment of C^* requires knowledge of the Poisson's ratio of foams υ_f. Since nanoindentation returns the reduced modulus E_r,

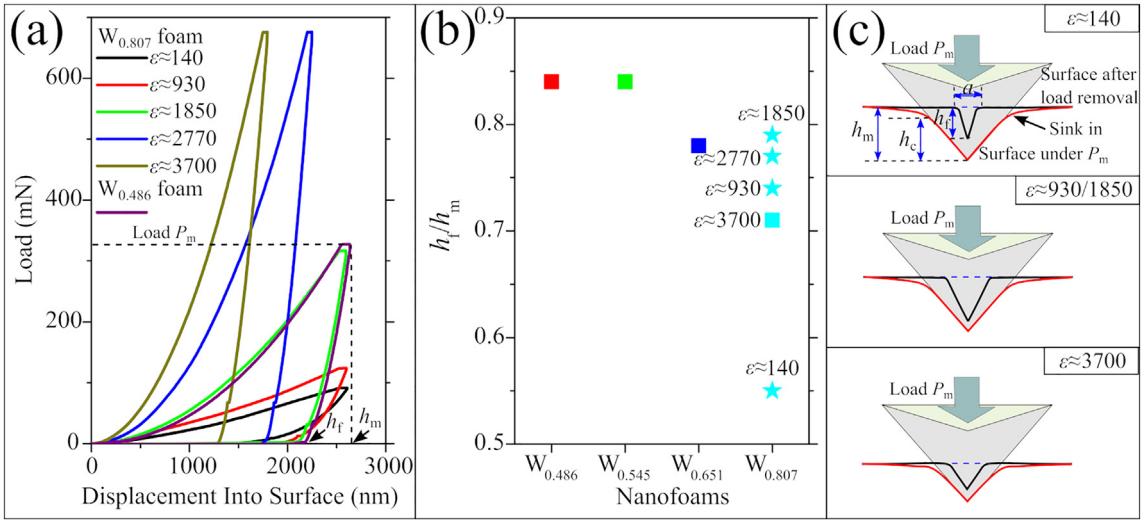

Fig. 4. Nanoindentation of the $W_{0.807}$ foams with various deformation strains and the $W_{0.486}$ nanofoams in the saturated region: (a) representative load-depth curves, (b) ratios between the penetration depth after load removal h_f and maximum penetration depth at peak load h_m, (c) schematic plots of indentation cross-sections (with a sink-in contact profile) made by a Berkovich indenter at the maximum peak load P_m and after load removal.

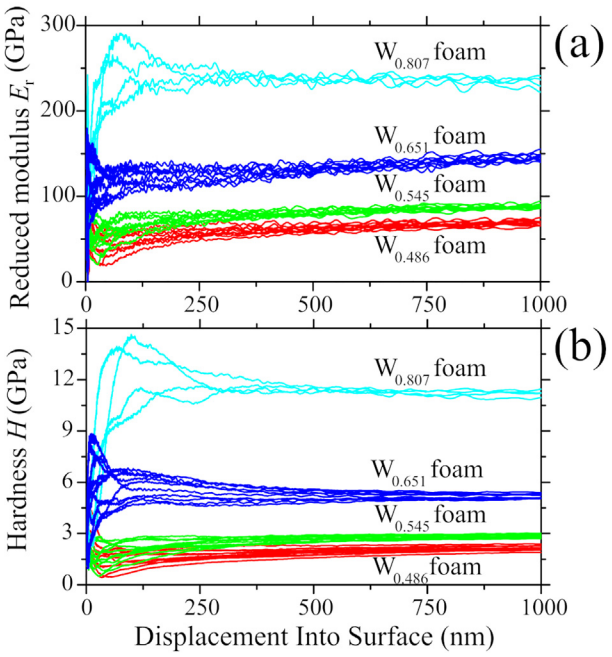

Fig. 5. Nanoindentation data showing (a) the reduced Young's modulus versus displacement curves, and (b) the hardness versus displacement data. For the $W_{0.807}$ nanofoam, experiments were conducted in the region with a deformation strain of about 3700. The nanoindentation for all the other W nanofoams was applied in the saturated regions.

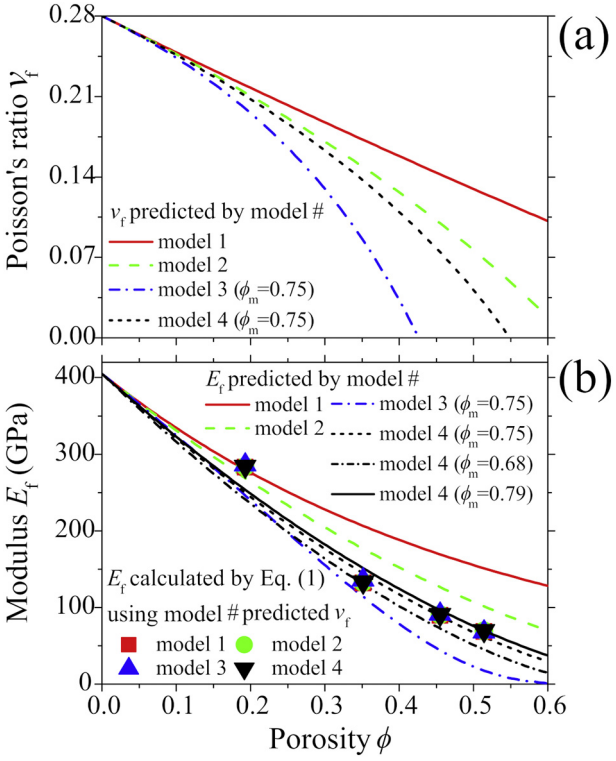

Fig. 6. Effective W nanofoam properties: (a) predicted Poisson's ratio υ_f versus porosity ϕ, (b) Young's modulus E_f versus porosity ϕ. A comparison between theoretical model predictions (Table 3) and the calculated data is presented in (b).

which involves elastic modulus and Poisson's ratio of a material (see Eq. (2)), an independent determination is not possible. Therefore, we employ model predictions from the four DEMA models listed in Table 3 to assess this quantity. As shown in Fig. 6a, different DEMA models give noticeably different predictions for υ_f. Surprisingly, as shown in Fig. 6b, the E_f calculated from the nanoindentation data by Eq. (2) using different predictions of υ_f are overlapping for each foam case, indicating the insensitivity of E_f to υ_f. The effective υ_f was then determined by the model equation giving the best description of the experimentally calculated E_f. For the $W_{0.807}$ nanofoam ($\phi = 0.193$) with $\varepsilon \approx 3700$, model 1 gives the best agreement. At higher porosities ($\phi > 0.3$), models 1 and 2 overpredict while model 3 underestimates the E_f of the W nanofoams. Model 4 provides a satisfactory description when using different ϕ_m values. With the gradual increase of ϕ from 0.349 to 0.514, the value of ϕ_m giving the best fit increases from 0.68 to 0.79. For random close packing of monosized spherical pores, ϕ_m is 0.637 [43]. The occurrence of an increase in ϕ_m suggests that W nanofoams with a porosity above 0.3 have polydisperse pore size distributions, which actually agrees well with the TEM observations in Fig. 2. Thus, for the remainder of this work, the υ_f values predicted by model 1 and model 4 with justified ϕ_m are adopted for the W nanofoams with $\phi = 0.193$ and $\phi > 0.3$, respectively. As shown in Table 4, the adopted υ_f value for all types of W nanofoams lies between 0 (for high-porosity W cellular solids) and 0.28 (for fully dense W). Accordingly, the C^* was estimated based on the relationship between C^* and υ_f [18]. It is noticed that the σ_f of W nanofoams reaches to levels of several GPa, which is about 3–15 times stronger than the widely investigated nanoporous Au foams [21,30].

To address the impact of foam structure on the mechanical behavior, Fig. 7a and b show the curves of the reduced Young's modulus E_r and the hardness H versus displacement for the $W_{0.807}$ foams with increasing deformation strains, i.e., with decreasing ligament sizes and decreasing structural disorders (see Fig. 3). Distinct variations in nanoindentation response are observed at small indentation depths, in particular for H. As the indenter continues to penetrate, E_r and H of foams with different deformation strains change noticeably with respect to the indentation depths. For the foams with $\varepsilon \leq 1850$, the nanoindentation properties drop gradually after initial data scattering and level off beyond 1800 nm. Contrarily, the nanoindentation properties of the foam with $\varepsilon \approx 2770$, especially the E_r, present an obvious rise after a short stabilization at depths between 500 and 750 nm. As previously described, the nanoindentation properties of the foam with $\varepsilon \approx 3700$ maintain at a high level after large data variations at small indentation depths. The average E_r and H values, taken from the plateau regions, are summarized in Fig. 7c. The standard deviations determined from four parallel indentation tests are shown in Fig. 7c as error bars. It is clearly seen that both quantities increase about one order of magnitude when the deformation strains increase from about 140 to 3700. Since the Poisson's ratios of foams υ_f decrease substantially with increasing structural disorders [47], E_f and σ_f of W foams with $\varepsilon \leq 2770$, where strongly disordered cellular structures prevail (see Fig. 4), are not provided here.

Table 4
Reduced Young's modulus E_r, Young's modulus E_f, hardness H, Poisson's ratio υ_f, constraint factor C^* and flow strength σ_f of the created W nanofoams.

Foams	E_r (GPa)	E_f (GPa)	H (GPa)	υ_f	C^*	σ_f (GPa)
$W_{0.807}$	236.1	284.3	11.2	0.220	2.9	3.9
$W_{0.651}$	120.8	132.6	5.3	0.128	2.6	2.0
$W_{0.545}$	84.7	90.3	2.8	0.074	2.3	1.2
$W_{0.486}$	65.7	67.3	2.0	0.027	1.8	1.1

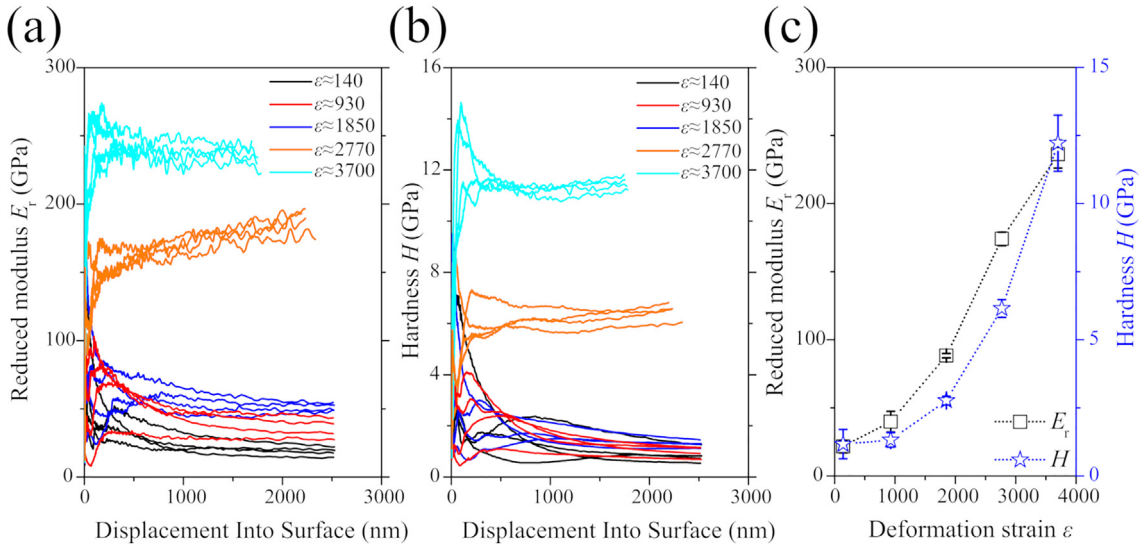

Fig. 7. $W_{0.807}$ foams received from the nanocomposite subjected to various deformation strains: (a) reduced Young's modulus versus displacement curves, (b) hardness versus displacement curves, (c) reduced modulus and hardness values against deformation strains.

4. Discussion

4.1. The modulus-structure relationship

Fig. 8 displays the relative Young's modulus of different W foams (E_f/E_s) as a function of the relative density φ. Owing to the insensitivity of E_f to υ_f, the reduced moduli of $W_{0.807}$ foams with $\varepsilon \lesssim 2770$ were calculated without considering the variation of ν_f resulted from the increasing structural disorders. That is, υ_f is taken as 0.220, which is determined for periodic pore-solid foams by using Eq. (2). The Reuss and Voigt bounds for pore-solid materials and the GA scaling law predictions for macroscopic open-cell foams are also plotted for comparison. It is evident that the E_f of all W foams lies between the Reuss and Voigt bounds. For the W nanofoams with self-similar and highly ordered cellular structures, the experimentally calculated E_f values are comparable to the GA scaling law predictions, suggesting that the elastic

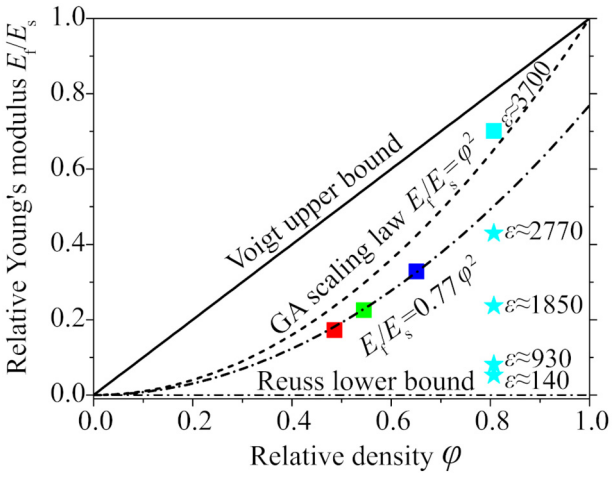

Fig. 8. Relative Young's modulus E_f/E_s with respect to relative density φ for the W foams with varying relative densities and cellular structures. The solid dots (red: $W_{0.486}$ foam, green: $W_{0.545}$ foam, blue: $W_{0.651}$ foam, cyan: $W_{0.807}$ foam) represent the experimentally calculated modulus values. The Voigt and Reuss bounds as well as the classical GA scaling law for macroscopic foams are plotted for comparison.

modulus of W foams is insensitive to the ligament sizes but dominantly depends on the relative density. This conclusion correlates well with previous research [28], underlining that the modulus of nanoporous materials is comparable to that of conventional macroscopic foams when the ligament thickness is above 20 nm. Since the theoretical GA structure-property relation is for ideal periodic models, which does not capture all the phenomena observable in the investigated W nanofoams (e.g. the geometrical arrangement of the cells, the shape of the cell struts and pores, presence of grain boundaries), it is up to expectations to observe a slight discrepancy between the experimentally calculated data and the GA scaling law predictions. In reality, the W nanofoams with $0.4 < \varphi < 0.7$ exhibiting a greater shape anisotropy of the cell struts (see Fig. 2) can be better described by a square power law with a proportional constant of 0.77 (see Fig. 8). This finding is in good agreement with GA's statement that the geometrical constants of proportionality depend on the actual shape anisotropy of the cell struts. Probably due to the remaining of 4.9 wt% Cu and the induced increase of relative density (~5.4%), the $W_{0.807}$ foam with $\varepsilon \approx 3700$ appears to have a measured modulus slightly higher than the GA's prediction. The $W_{0.807}$ foam with a high deformation strain is much different from the $W_{0.807}$ foam with a low deformation strain in microstructure (see Fig. 3), including grain sizes, ligament thicknesses and structural disorders. But structural disorders are regarded as the dominant factors contributing to the reduction of foam modulus, as grain sizes [48–50] and ligament thicknesses [24–27] were demonstrated previously to have little impact on the foam modulus when they are above 20 nm.

4.2. The strength-structure relationship

Fig. 9a shows the dependence of flow strength σ_f on the relative density φ for the W nanofoams with self-similar and highly ordered cellular structures. All strength values experimentally determined from hardness lie between the Reuss and Voigt bounds. Three well established scaling law equations (see Table 1) are employed to describe the experimental strength values. Models used to derive Reuss and Voigt bounds and the GA scaling equations are depicted in Fig. 9b for a better understanding. Here it is worth to mention that, to simplify the calculation, the input ligament thickness t in the GA-H and GA-FF scaling equations is 25 nm for all W nanofoam cases. Such a treatment undoubtedly overestimates the strength of $W_{0.807}$ nanofoam with $t = 28$ nm, and meanwhile underestimates the strength of $W_{0.486}$ and $W_{0.545}$ nanofoams

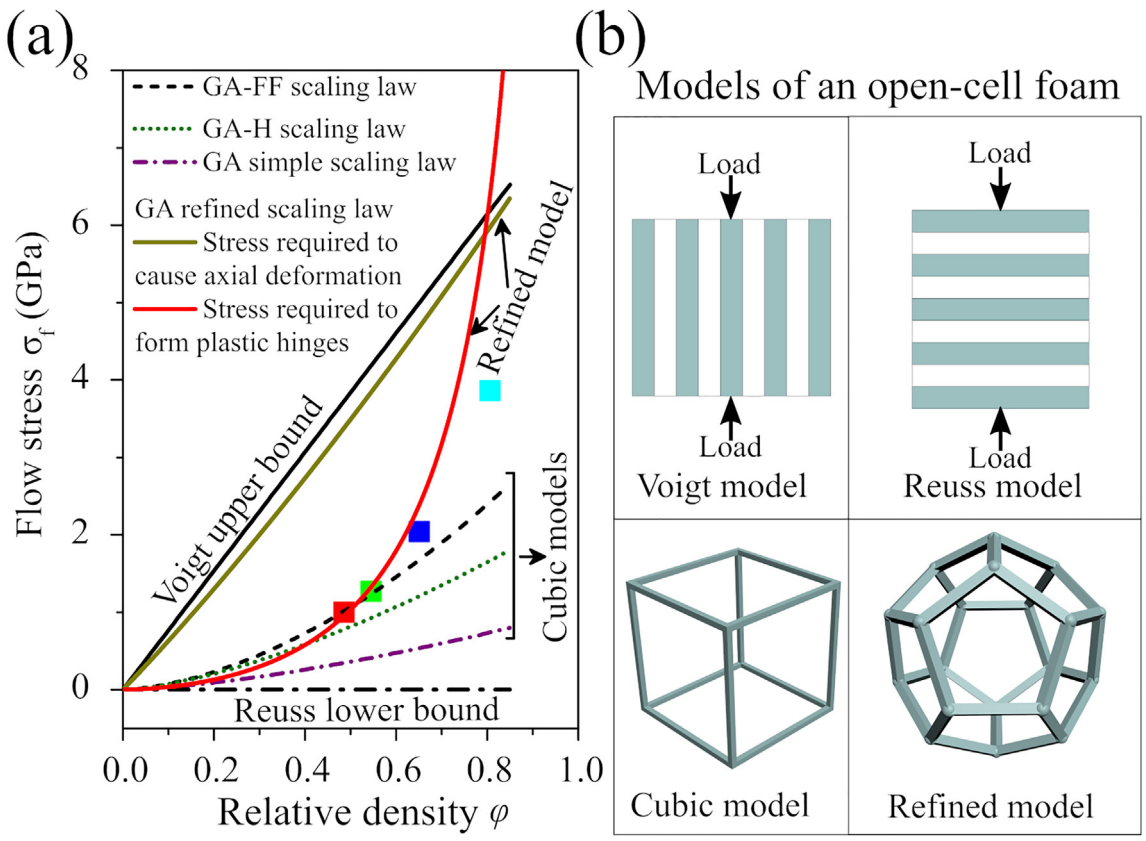

Fig. 9. (a) Relative density dependence of flow strength for the W nanofoams with self-similar and highly ordered cellular structures. The solid squares represent the experimentally calculated strength values. The flow strength predicted by different GA scaling laws and Reuss-Voigt bounds are provided as a comparison. (b) Models applied to obtain different theoretical predictions.

probably with $t < 25$ nm. However, the deviation produced by simply using $t = 25$ nm is very insignificant and can even be neglected. The flow strength of solid bulk W used in the GA simple scaling equation is taken as 3.4 GPa [31]. Apparently, the GA-FF scaling law $\sigma_f = 0.23\varphi^{3/2}(1+\varphi^{1/2})(\sigma + kt^{-1/2})$ [30], which not only highlights the importance of relative density and ligament size, but also includes corrections to the relative density equation, gives the best description to the experimental data. However, this scaling law is no longer valid for the W nanofoam with a relative density as high as 0.651 and 0.807. As suggested from GA's work, the discrepancy between the experimental data and scaling law predictions is caused by reality, as the cubic model (see Fig. 9b) is no longer a good approximation for the cell shape of the realistic foams with relative densities above 0.6. To overcome the deficiencies of the cubic model, GA employed a refined pentagonal dodecahedral model (see Fig. 9b) to recalculate the foam properties. As observed in Fig. 9a, the refined model outputs two strength-density curves, corresponding respectively to the collapse stress required to form plastic hinges at the cell edges (see the solid red curve) and to cause yielding of the axially loaded cell members (see the solid yellow curve). The scaling expression (see Table 1) for the stress required to form plastic hinges gives a good description for the W nanofoams with $\varphi = 0.486$ and 0.545 when taking the constant of proportionality C as 0.14. Despite altering of the plastic collapse mechanisms, the refined model outputs collapse stresses higher than the cubic models, giving a possible explanation for the high strength values of the $W_{0.651}$ and $W_{0.807}$ nanofoams. The detected high amount of Cu (4.9 wt%, see Figs. S3f and 5) and thereby induced increase of relative density (by 5.4%) are probably additional factors contributing to the exceptional high modulus of the $W_{0.807}$ nanofoam. Here it is worth to mention that, in terms of predicting the flow stress of a pore-solid composite, the Voigt upper bound derived from the axial loading of a lamella model is quite comparable to the refined scaling expression for the stress required to cause axial deformation of a pentagonal dodecahedral cell.

The constraint factor C^* decreases strongly with the decrease of υ_f [18], making it difficult to calculate accurately the flow strength σ_f of the $W_{0.807}$ foams with various cellular structures by using Eq. (3). Thus, we refrain from quantitative assessments of the influence of structural imperfection on strength of nanofoams. However, qualitatively it can be stated that the deterioration of the flow strength in the $W_{0.807}$ foams should be correlated with their structural details, including the changing grain sizes, ligament thicknesses and structural disorders.

4.3. Structural architecture dependence of nanoindentation response

Fig. 10 shows the schematic drawing of nanoindentation tests on the $W_{0.807}$ foams with various cellular structures. The structural characteristics of the $W_{0.807}$ foams with different deformation strains along the loading direction are captured from Fig. 3 of this work and Fig. 3 of Ref. [37]. The plastically and elastically deformed zones, from where the foam properties are originated, are marked inside and out the red dashed lines, respectively. Please note that the size of the plastic zone beneath a Berkovich tip (z_{ys}) can be estimated using a well known expression, which is based on the assumption of an expanding spherical cavity and considers the flow strength σ and the elastic modulus E [51,52]:

$$\frac{z_{ys}}{h_s} = \left(\frac{2E}{3\sigma}\right)^{1/3} \tag{4}$$

Here, h_s represents for the penetration depth. With the foam properties listed in Table 4, the plastic zone is calculated to be ~3–4 times

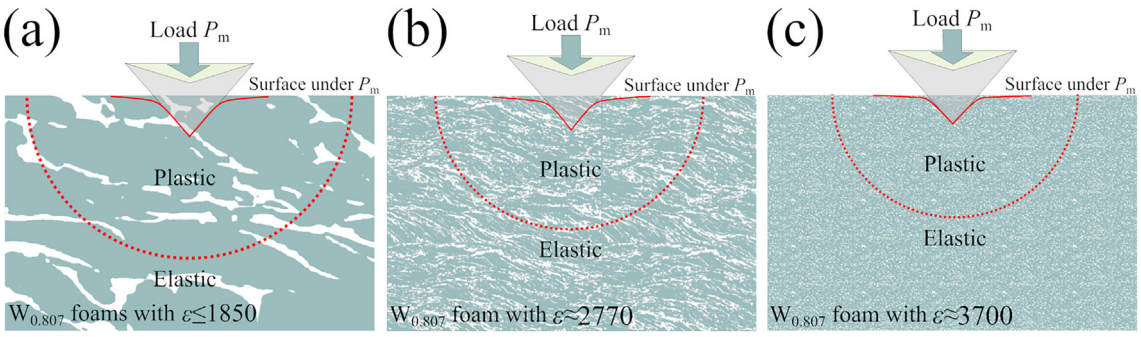

Fig. 10. Schematic drawing of nanoindentation tests on the $W_{0.807}$ foams (blue: W ligaments; white: pores) with: (a) $\varepsilon \leq 1850$, corresponding to an elongated and (sub)-micrometer cellular morphology, (b) $\varepsilon \approx 2770$, corresponding to an elongated and nanometer cellular morphology, (c) $\varepsilon \approx 3700$, corresponding to an equiaxed/spherical and nanometer cellular morphology. A plastic deformation zone beneath the indenter is inside the red dashed line. SEM images of the cross-sections showing the sub-surface microstructures and plastic zones of the $W_{0.807}$ foams with $\varepsilon \approx 1850$ and $\varepsilon \approx 2770$ are available in Figs. S7 and 8.

radially around the indenter for the W nanofoams with various relative densities. In the SEM images of the cross-sections (see Figs. S7d and 8b), the $W_{0.807}$ foams with $\varepsilon \approx 1850$ and 2770 appear to have plastic zone sizes of about 4 and 3.7 times of their respective maximum penetration depths h_m, demonstrating convincingly the validity of Eq. (4) in the estimation of the plastic zone sizes of W foam materials. As illustrated in Fig. 10a, the $W_{0.807}$ foams with $\varepsilon \leq 1850$ are composed of W ligaments with a thickness on a (sub)-micrometer scale (see Figs. 3a–3c), resulting in a rather inhomogeneous distribution of pores and ligaments within both the plastically and elastically deformed regions. It means that not only the position where the indenter starts to penetrate but also the depth that the indenter penetrates to have noticeable impacts on the evaluation of foam properties using depth-sensing nanoindentation. Therefore, a strong scattering of foam properties among the four parallel indentation tests are observed in Fig. 7. Contrarily, the ligaments of the $W_{0.807}$ foams with $\varepsilon \approx 2770$ and 3700 are at nanoscale (see Fig. 3d and e), ensuring the sensing of an ensemble of ligaments and pores instead of individual ligaments at very shallow penetration depths, and thus allowing low property variations among the four nanoindentation tests.

As shown in Fig. 7, after distinct variations of foam properties at small indentation depths, the $W_{0.807}$ foams with different deformation strains exhibit a different changing trend against the penetration depths. Such a phenomenon should be closely correlated with the cellular structure details, as foam bending/yielding is strongly influenced by the cellular shapes [53,54]. That is, cells that are elongated normal to the loading direction are comparatively weaker than equiaxed/spherical cells. As depicted in Fig. 10, the $W_{0.807}$ foams with $\varepsilon \approx 2770$ exhibit elongated cellular structure normal to the loading direction (for the real structural features, please see Fig. S8), whereas the unit cells in the $W_{0.807}$ foams with $\varepsilon \approx 3700$ are equiaxed/spherical. When exposed to mechanical stress, the elongated cells in the $W_{0.807}$ foams with $\varepsilon \approx 2770$ are prone to experience large permanent plastic bending and promote densification at the early stage of the loading process, thus inducing a noticeable apparent strain hardening for penetration depths above 750 nm (Fig. 7). Contrarily, due to the difficult densification of the equiaxed/spherical cells, a plateau region with a high modulus/hardness value and a wide depth range appears during nanoindentation tests on the $W_{0.807}$ foams with $\varepsilon \approx 3700$ (Fig. 7). The cells in the $W_{0.807}$ foams with $\varepsilon \leq 1850$ also exhibit an elongated morphology normal to the loading direction (for an insight image, please see Fig. 3 in Ref. [37] or Fig. S7 in the Supplementary Information). However, because of their (sub)-micrometer scaled ligaments, a plateau region with a low modulus/hardness value is achieved at a very late stage of loading process [55], i.e., at the penetration depths above 1800 nm. Under the circumstance that the foam properties at small penetration depths are overestimated due to the indentation size effects [52], a decay of foam properties with increasing penetration depths occurs before reaching the plateau region.

Unlike the $W_{0.807}$ nanofoam with $\varepsilon \approx 3700$ (Fig. 2b), which has narrowly-distributed spherical pores/cells as a dominant feature, the W nanofoams with decreasing relative densities ($\varphi = 0.651$, 0.545, 0.486) are characterized with increasing amount of poly-dispersed elliptical pores/cells (Fig. 2a). Besides, in comparison to the $W_{0.807}$ nanofoam with $\varepsilon \approx 3700$ (Fig. 3d), the anisotropic level of the pores/cells in the W nanofoams with $\varphi = 0.651$, 0.545, 0.486 are more significant. Thus, during the nanoindentation loading process, it is up to expectations to observe in Fig. 5 that the W nanofoams with decreasing relative densities exhibit a faint but non-negligible rise of the foam properties with the increasing penetration depths.

5. Conclusions

In this work, the mechanical response of polycrystalline tungsten nanofoams with independently varied relative densities (ranging from 0.484 to 0.807) and cellular structures was investigated by employing depth-sensing nanoindentation tests. We observed that, for tungsten nanofoams maintaining self-similar and highly ordered cellular structures, the elastic modulus varied with relative density in a close way to the classical Gibson-Ashby scaling law, demonstrating the insensibility of elastic modulus to ligament thickness. The flow strength of the tungsten nanofoams can be better described by a refined scaling law, which not only highlights the importance of relative density but also incorporates ligament size effects and corrections to the equation of relative density. However, since cubic models are no longer a good approximation for the cell shape of foams with a relative density above 0.6, a discrepancy between the experimentally calculated data and the refined scaling law predictions was observed for the tungsten nanofoams with high relative densities. The mechanical response of the tungsten foams with varied cellular structures revealed that both, the stiffness and strength of the open cell tungsten nanofoams, were deteriorated by increasing structural disorders. At the end, the deformation behavior of the investigated W foams under nanoindentation loading was discussed by taking into account the effects of the solid cell shapes and ligament thicknesses. In comparison to the equiaxed/spherical solid cells, cells that are elongated normal to the loading direction are more prone to bend plastically and to promote densification of the foams. The elongated cells with nanometer sizes are generally stiffer and stronger than the elongated cells with (sub)-micrometer sizes.

This work unveils not only the potential to tailor properties of nanofoams, but also some limitations of established scaling laws for describing the mechanical properties of the newly created nanoporous tungsten foams. Our findings highlight how the structural details (including relative density, cell shape anisotropy, ligament thickness, and

structural disorder) influence the mechanical performance of metallic foams, thereby providing a valuable structural optimization guide for producing cellular solids with specific end-use properties. The unique fabrication route of metallic nanofoams, i.e., high pressure torsion of coarse-grained metallic composites together with selective dissolution of sacrificial phases, is shown to be an effective avenue in the elimination of large cells, meanwhile avoiding cells with strong shape anisotropy. In fact, the strength of the tungsten nanofoams reaches up to a level of several GPa, exhibiting a great potential to satisfy the need for advanced high performance materials that can endure harsh environments.

Declaration of Competing Interest

None.

Acknowledgments

This work is funded by the Austrian Science Fund (FWF) under Lise Meitner project No. M 2405-N36 (IRRESIST). The authors kindly acknowledge the financial support by the European Research Council (ERC) under the grant No. 771146 (TOUGHIT), and by the Austrian Federal Ministries for Transport, Innovation and Technology (BMVIT) and for Digital and Economic Affairs (BMDW), represented by the Österreichische Forschungsförderungsgesellschaft (Funder ID: 10.13039/501100004955), and the federal states of Styria, Upper Austria, and Tyrol within the framework of the COMET K2 Funding Program IC-MPPE (No. 859480) is also gratefully acknowledged. The authors would like to thank Jinming Guo for the TEM imaging in Fig. 2b.

Data availability

The raw/processed data required to reproduce these findings will be shared with interested parties upon reasonable request.

Appendix A. Supplementary data

Supplementary data to this article can be found online at https://doi.org/10.1016/j.matdes.2020.109187.

References

[1] Y. Ding, Y.J. Kim, J. Erlebacher, Nanoporous gold leaf: "ancient technology"/advanced material, Adv. Mater. 16 (2004) 1897–1900, https://doi.org/10.1002/adma.200400792.

[2] L. Chen, J. Yu, T. Fujita, M. Chen, Nanoporous copper with tunable nanoporosity for SERS applications, Adv. Funct. Mater. 19 (2009) 1221–1226, https://doi.org/10.1002/adfm.200801239.

[3] H. Jin, X. Wang, S. Parida, K. Wang, M. Seo, J. Weissmüller, Nanoporous Au—Pt alloys as large strain electrochemical actuators, Nano Lett. 10 (2010) 187–194, https://doi.org/10.1021/nl903262b.

[4] T. Déronzier, F. Morfin, L. Massin, M. Lomello, J. Rousset, Pure nanoporous gold powder: synthesis and catalytic properties, Chem. Mater. 23 (2011) 5287–5289, https://doi.org/10.1021/cm202105k.

[5] M.M. Biener, J. Biener, A. Wichmann, A. Wittstock, T.F. Baumann, M. Bäumer, A.V. Hamza, ALD functionalized nanoporous gold: thermal stability, mechanical properties, and catalytic activity, Nano Lett. 11 (2011) 3085–3090, https://doi.org/10.1021/nl200993.

[6] H.J. Qiu, J.L. Kang, P. Liu, A. Hirata, T. Fujita, M.W. Chen, Fabrication of large-scale nanoporous nickel with a tunable pore size for energy storage, J. Power Sources 247 (2014) 896–905, https://doi.org/10.1016/j.jpowsour.2013.08.070.

[7] M.D. Uchic, D.M. Dimiduk, J.N. Florando, W.D. Nix, Sample dimensions influence strength and crystal plasticity, Science 305 (2004) 986, https://doi.org/10.1126/science.1098993.

[8] J.R. Greer, W.C. Oliver, W.D. Nix, Size dependence of mechanical properties of gold at the micron scale in the absence of strain gradients, Acta Mater. 53 (2005) 1821–1830, https://doi.org/10.1016/j.actamat.2004.12.031.

[9] E.M. Bringa, J.D. Monk, A. Caro, A. Misra, L. Zepeda-Ruiz, M. Duchaineau, F. Abraham, M. Nastasi, S.T. Picraux, Y.Q. Wang, D. Farkas, Are nanoporous materials radiation resistant? Nano Lett. 12 (2012) 3351–3355, https://doi.org/10.1021/nl201383u.

[10] C. Sun, D. Bufford, Y. Chen, M.A. Kirk, Y.Q. Wang, M. Li, H. Wang, S.A. Maloy, X. Zhang, In situ study of defect migration kinetics in nanoporous Ag with enhanced radiation tolerance, Sci. Rep. 4 (2014) 3737, https://doi.org/10.1038/srep03737.

[11] J. Li, C. Fan, J. Ding, S. Xue, Y. Chen, Q. Li, H. Wang, X. Zhang, In situ heavy ion irradiation studies of nanopore shrinkage and enhanced radiation tolerance of nanoporous Au, Sci. Rep. 7 (2017) 39484, https://doi.org/10.1038/srep39484.

[12] M. Rieth, S.L. Dudarev, S.M. Gonzalez De Vicente, J. Aktaa, T. Ahlgren, S. Antusch, D.E.J. Armstrong, M. Balden, N. Baluc, M.F. Barthe, W.W. Basuki, M. Battabyal, C.S. Becquart, D. Blagoeva, H. Boldyryeva, J. Brinkmann, M. Celino, L. Ciupinski, J.B. Correia, A. De Backer, C. Domain, E. Gaganidze, C. García-Rosales, J. Gibson, M.R. Gilbert, S. Giusepponi, B. Gludovatz, H. Greuner, K. Heinola, T. Höschen, A. Hoffmann, N. Holstein, F. Koch, W. Krauss, H. Li, S. Lindig, J. Linke, C. Linsmeier, P. López-Ruiz, H. Maier, J. Matejicek, T.P. Mishra, M. Muhammed, A. Muñoz, M. Muzyk, K. Nordlund, D. Nguyen-Manh, J. Opschoor, N. Ordás, T. Palacios, G. Pintsuk, R. Pippan, J. Reiser, J. Riesch, S.G. Roberts, L. Romaner, M. Rosiński, M. Sanchez, W. Schulmeyer, H. Traxler, A. Ureña, J.G. van der Laan, L. Veleva, S. Wahlberg, M. Walter, T. Weber, T. Weitkamp, S. Wurster, M.A. Yar, J.H. You, A. Zivelonghi, Recent progress in research on W materials for nuclear fusion applications in Europe, J. Nucl. Mater. 432 (2013) 482–500, https://doi.org/10.1016/j.jnucmat.2012.08.018.

[13] S.J. Zinkle, G.S. Was, Materials challenges in nuclear energy, Acta Mater. 61 (2013) 735–758, https://doi.org/10.1016/j.actamat.2012.11.004.

[14] S.J. Zinkle, L.L. Snead, Designing radiation resistance in materials for fusion energy, Annu. Rev. Mater. Res. 44 (2014) 241–267, https://doi.org/10.1146/annurev-matsci-070813-113627.

[15] O. El-Atwani, J.A. Hinks, G. Greaves, S. Gonderman, T. Qiu, M. Efe, J.P. Allain, In-situ TEM observation of the response of ultrafine- and nanocrystalline-grained tungsten to extreme irradiation environments, Sci. Rep. 4 (2014) 4716, https://doi.org/10.1038/srep04716.

[16] W. Voigt, Über die Beziehung zwischen den beiden Elasticitätsconstanten isotroper Körper, Ann. Phys. Berlin 274 (1889) 573–587, https://doi.org/10.1002/andp.18892741206.

[17] A. Reuss, Berechnung der Fließgrenze von Mischkristallen auf Grund der Plastizitätsbedingung für Einkristalle, J. Appl. Math. Mech./, Z. Angew. Math. Mech. 9 (1929) 49–58, https://doi.org/10.1002/zamm.19290090104.

[18] L.J. Gibson, M.F. Ashby, Cellular Solids: Structure and Properties, Cambridge University Press, Cambridge, UK, 1997https://doi.org/10.1017/CBO9781139878326.

[19] M.F. Ashby, R.F.M. Medalist, The mechanical properties of cellular solids, Metall. Trans. A. 14 (1983) 1755–1769, https://doi.org/10.1007/BF02645546.

[20] I.J. Gibson, M.F. Ashby, The mechanics of three-dimensional cellular materials, Proc. Roy. Soc. Lond. Math. Phys. Sci. 382 (1982) 43–59, https://doi.org/10.1098/rspa.1982.0088.

[21] A.M. Hodge, J. Biener, J.R. Hayes, P.M. Bythrow, C.A. Volkert, A.V. Hamza, Scaling equation for yield strength of nanoporous open–cell foams, Acta Mater. 55 (2007) 1343–1349, https://doi.org/10.1016/j.actamat.2006.09.038.

[22] N. Huber, R.N. Viswanath, N. Mameka, J. Markmann, J. Weißmüller, Scaling laws of nanoporous metals under uniaxial compression, Acta Mater. 67 (2014) 252–265, https://doi.org/10.1016/j.actamat.2013.12.003.

[23] K.R. Mangipudi, E. Epler, C.A. Volkert, Topology-dependent scaling laws for the stiffness and strength of nanoporous gold, Acta Mater. 119 (2016) 115–122, https://doi.org/10.1016/j.actamat.2016.08.012.

[24] R. Liu, R.A. Antoniou, A relationship between the geometrical structure of a nanoporous metal foam and its modulus, Acta Mater. 61 (2013) 2390–2402, https://doi.org/10.1016/j.actamat.2013.01.011.

[25] G. Pia, M. Carta, F. Delogu, Nanoporous Au foams: variation of effective Young's modulus with ligament size, Scripta Mater. 144 (2018) 22–26, https://doi.org/10.1016/j.scriptamat.2017.09.038.

[26] S. Mathesan, D. Mordehai, Size-dependent elastic modulus of nanoporous Au nanopillars, Acta Mater. 185 (2020) 441–452, https://doi.org/10.1016/j.actamat.2019.12.018.

[27] A. Mathur, J. Erlebacher, Size dependence of effective Young's modulus of nanoporous gold, Appl. Phys. Lett. 90 (2007) 61910, https://doi.org/10.1063/1.2436718.

[28] N. Mameka, J. Markmann, H.J. Jin, J. Weissmuller, Electrical stiffness modulation-confirming the impact of surface excess elasticity on the mechanical of nanomaterials, Acta Mater. 76 (2014) 272–280, https://doi.org/10.1016/j.actamat.2014.04.067.

[29] X. Sun, G. Xu, X. Li, X. Feng, H. Gao, Mechanical properties and scaling laws of nanoporous gold, J. Appl. Phys. 113 (2013) 23505, https://doi.org/10.1063/1.4774246.

[30] H.L. Fan, D.N. Fang, Modeling and limits of strength of nanoporous foam, Mater. Design 30 (2009) 1441–1444, https://doi.org/10.1016/j.matdes.2008.08.011.

[31] M. Zhao, I. Issa, M.J. Pfeifenberger, M. Wurmshuber, D. Kiener, Tailoring ultra-strong nanocrystalline tungsten nanofoams by reverse phase dissolution, Acta Mater. 182 (2020) 215–225, https://doi.org/10.1016/j.actamat.2019.10.030.

[32] M.J. Silva, W.C. Hayes, L.J. Gibson, The effects of non-periodic microstructure on the elastic properties of two-dimensional cellular solids, Int. J. Mech. Sci. 37 (1995) 1161–1177, https://doi.org/10.1016/0020-7403(94)00018-F.

[33] A.E. Simone, L.J. Gibson, Effects of solid distribution on the stiffness and strength of metallic foams, Acta Mater. 46 (1998) 2139–2150, https://doi.org/10.1016/S1359-6454(97)00421-7.

[34] X.E. Guo, L.J. Gibson, Behavior of intact and damaged honeycombs: a finite element study, Int. J. Mech. Sci. 41 (1999) 85–105, https://doi.org/10.1016/S0020-7403(98)00037-X.

[35] H.X. Zhu, J.R. Hobdell, A.H. Windle, Effects of cell irregularity on the elastic properties of open-cell foams, Acta Mater. 48 (2000) 4893–4900, https://doi.org/10.1016/S1359-6454(00)00282-2.
[36] K.S. Kormout, R. Pippan, A. Bachmaier, Deformation–induced supersaturation in immiscible material systems during high–pressure torsion, Adv. Eng. Mater. 19 (2017) 1600675, https://doi.org/10.1002/adem.201600675.
[37] I. Sabirov, R. Pippan, Formation of a W–25% Cu nanocomposite during high pressure torsion, Scripta Mater. 52 (2005) 1293–1298, https://doi.org/10.1016/j.scriptamat.2005.02.017.
[38] H.P. Stüwe, Equivalent strains in severe plastic deformation, Adv. Eng. Mater. 5 (2003) 291–295, https://doi.org/10.1002/adem.200310085.
[39] W.C. Oliver, G.M. Pharr, An improved technique for determining hardness and elastic modulus using load and displacement sensing indentation experiments, J. Mater. Res. 7 (1992) 1564–1583, https://doi.org/10.1557/JMR.1992.1564.
[40] D. Kramer, H. Huang, M. Kriese, J. Robach, J. Nelson, A. Wright, D. Bahr, W.W. Gerberich, Yield strength predictions from the plastic zone around nanocontacts, Acta Mater. 47 (1998) 333–343, https://doi.org/10.1016/S1359-6454(98)00301-2.
[41] S.S. Chiang, D.B. Marshall, A.G. Evans, The response of solids to elastic/plastic indentation. I. Stresses and residual stresses, J. Appl. Phys. 53 (1982) 298–311, https://doi.org/10.1063/1.329930.
[42] A. Leitner, V. Maier-Kiener, J. Jeong, M.D. Abad, P. Hosemann, S.H. Oh, D. Kiener, Interface dominated mechanical properties of ultra-fine grained and nanoporous Au at elevated temperatures, Acta Mater. 121 (2016) 104–116, https://doi.org/10.1016/j.actamat.2016.08.071.
[43] R. Pal, Porosity-dependence of effective mechanical properties of pore-solid composite materials, J. Compos. Mater. 39 (2005) 1147–1158, https://doi.org/10.1177/0021998305048744.
[44] A. Bolshakov, G.M. Pharr, Influences of pileup on the measurement of mechanical properties by load and depth sensing indentation techniques, J. Mater. Res. 13 (1998) 1049–1058, https://doi.org/10.1557/JMR.1998.0146.
[45] W.D. Nix, H.J. Gao, Indentation size effects in crystalline materials: a law for strain gradient plasticity, J. Mech. Phys. Solids 46 (1998) 411–425, https://doi.org/10.1016/S0022-5096(97)00086-0.
[46] J.G. Swadener, E.P. George, G.M. Pharr, The correlation of the indentation size effect measured with indenters of various shapes, J. Mech. Phys. Solids 50 (2002) 681–694, https://doi.org/10.1016/S0022-5096(01)00103-X.
[47] B. Roschning, N. Huber, Scaling laws of nanoporous gold under uniaxial compression: effects of structural disorder on the solid fraction, elastic Poisson's ratio, Young's modulus and yield strength, J. Mech. Phys. Solids 92 (2016) 55–71, https://doi.org/10.1016/j.jmps.2016.02.018.
[48] H.S. Kim, M.B. Bush, The effects of grain size and porosity on the elastic modulus of nanocrystalline materials, Nanostruct. Mater. 11 (1999) 361–367, https://doi.org/10.1016/S0965-9773(99)00052-5.
[49] J.D. Giallonardo, U. Erb, K.T. Aust, G. Palumbo, The influence of grain size and texture on the Young's modulus of nanocrystalline nickel and nickel–iron alloys, Philos. Mag. 91 (2011) 4594–4605, https://doi.org/10.1080/14786435.2011.615350.
[50] P. Valat-Villain, J. Durinck, P.O. Renault, P. Xiao, Grain size dependence of elastic moduli in nanocrystalline tungsten, J. Nanomater. 2017 (2017) 3620910, https://doi.org/10.1155/2017/3620910.
[51] R. Hill, The Mathematical Theory of Plasticity, Oxford University Press, Oxford, UK, 1950.
[52] C.K. Dolph, D.J. Da Silva, M.J. Swenson, J.P. Wharry, Plastic zone size for nanoindentation of irradiated Fe–9%Cr ODS, J. Nucl. Mater. 481 (2016) 33–45, https://doi.org/10.1016/j.jnucmat.2016.08.033.
[53] H. Bart-Smith, A.F. Bastawros, D.R. Mumm, A.G. Evans, D.J. Sypeck, H.N.G. Wadley, Compressive deformation and yielding mechanisms in cellular Al alloys determined using X-ray tomography and surface strain mapping, MRS Proc. 521 (1998) 71, https://doi.org/10.1557/PROC-521-71.
[54] M. Tane, R. Okamoto, H. Nakajima, Tensile deformation of anisotropic porous copper with directional pores, J. Mater. Res. 25 (2010) 1975–1982, https://doi.org/10.1557/JMR.2010.0261.
[55] Y. Kim, E. Gwak, S. Ahn, J. Jang, H.N. Han, J. Kim, Indentation size effect in nanoporous gold, Acta Mater. 138 (2017) 52–60, https://doi.org/10.1016/j.actamat.2017.07.040.